

Impact Dynamics of Moons Within a Planetary Potential

R. Rufu^{1,2} and O. Aharonson^{1,3}

¹Weizmann Institute of Science, Department of Earth and Planetary Sciences, Rehovot, Israel

²Southwest Research Institute, 1050 Walnut Street, Suite 300, Boulder, CO 80302, USA

³Planetary Science Institute, Tucson, AZ, USA

Key Points:

- Impacts within the planetary potential are more erosive.
- Dynamical studies of the evolution of multiple satellite, must consider fragmentation.
- Significant portions of the lunar mantle are melted during a companion impact.

arXiv:1904.02105v2 [astro-ph.EP] 4 Apr 2019

Corresponding author: R. Rufu, raluca@boulder.swri.edu

Abstract

Current lunar origin scenarios suggest that Earth’s Moon may have resulted from the merger of two (or more) smaller moonlets. Dynamical studies of multiple moons find that these satellite systems are not stable, resulting in moonlet collision or loss of one or more of the moonlets. We perform Smoothed Particle Hydrodynamic (SPH) impact simulations of two orbiting moonlets inside the planetary gravitational potential and find that the classical outcome of two bodies impacting in free space is altered as erosive mass loss is more significant with decreasing distance to the planet. Depending on the conditions of accretion, each moonlet could have a distinct isotopic signature, therefore, we assess the initial mixing during their merger, in order to estimate whether future measurements of surface variations could distinguish between lunar origin scenarios (single vs. multiple moonlets). We find that for comparable-size impacting bodies in the accretionary regime, surface mixing is efficient, but in the hit-and-run regime, only small amount of material is transferred between the bodies. However, sequences of hit-and-run impacts are expected, which will enhance the surface mixing. Overall, our results show that large scale heterogeneities can arise only from the merger of drastically different component masses. Surfaces of moons resulting from merger of comparable-sized components have little material heterogeneities, and such impacts are preferred, as the relatively massive impactor generates more melt, extending the lunar magma ocean phase.

Plain Language Summary

Lunar origin scenarios suggest that Earth’s single Moon may be a result of merger between smaller moonlets. In this work we test different impact scenarios of two orbiting moonlets, and include the effect of Earth’s gravitational potential. We find that impacts within Earth’s gravitational potential are different from impacts of two bodies in free space. For example, the amount of debris generated during such impacts is enhanced, and thus the mass retained in the final Moon is smaller than previously estimated. As each moonlet could inherit distinct isotopic signature, we test the initial surface mixing between the two components, in order to estimate whether future measurements of surface variation could differentiate between lunar origin theories. We find that surfaces of moonlets resulting from the merger of two comparable-size components are efficiently mixed. For the origin of the Moon, comparable-sized components are preferred, as they are able to generate enough melt and extend the lunar magma ocean phase to be compatible with the observed lunar crust.

1 Introduction

Impacts between two orbiting satellites may be an integral part of satellite formation and specifically lunar formation. Mergers between moonlets are especially interesting for the newly proposed multiple-impact hypothesis as these moonlets form from different debris disks and merge together to form the final Moon [Rufu *et al.*, 2017]. However, this process is also relevant for the single giant impact, as previous work shows that multiple moonlets can form from the same debris disk [Ida *et al.*, 1997; Salmon and Canup, 2012, 2014].

Satellite pairs were found to be mostly unstable [Canup *et al.*, 1999; Citron *et al.*, 2018], leading to moonlet-moonlet collisions or the loss of one (or both) of the moonlets. In the context of the canonical giant impact, where two moonlets are accreted in the same debris disk, merging occurs rapidly when the inner moonlet is larger than the outer moonlet [Canup *et al.*, 1999]. In the context of the multiple impact hypothesis, Citron *et al.* [2018] demonstrated that a preexisting moonlet can remain stable during subsequent impacts onto the protoplanet and later merge with the newly accreted moonlet. While these studies were able to evaluate the dynamical evolution of the two moonlets up to their impact, they do not estimate the impact outcome, and rather

assume perfect merger of the two components. However, the collisional outcomes vary substantially from perfect merger of the two colliding bodies at low velocities, to hit-and-run where the two bodies graze each other but have sufficient relative velocity to escape the mutual gravitational well [Leinhardt and Stewart, 2012]. In the hit-and-run regime little mass is transferred between the two colliding bodies.

The dynamics of impacts between two orbiting bodies is substantially different from previously heavily studied planetary-sized impacts [Hartmann and Davis, 1975; Cameron and Ward, 1976; Benz et al., 1989; Canup and Asphaug, 2001; Canup, 2004a, 2008; Čuk and Stewart, 2012; Canup, 2012; Rufu et al., 2017; Lock et al., 2018]. Firstly, for orbiting sub-lunar mass bodies around Earth, the impact velocities are smaller and limited to ~ 1 km/s, thus heating is limited. Secondly, multiple satellite systems that typically lead to close encounters are moonlets with comparable sizes [Canup et al., 1999]. Therefore, moonlet-moonlet collisions offer an interesting, and only marginally explored, impact size-distribution [Canup, 2005; Asphaug, 2010] where both moonlets would contribute similarly and substantially to the final satellite, as opposed to the planetary-scale impacts, that were thoroughly studied in the context of the Moon formation [Benz et al., 1989; Canup, 2004a; Čuk and Stewart, 2012; Rufu et al., 2017]. Thirdly, in the context of planetary scale impacts the solar tidal environment is neglected because the planetary Hill sphere is substantially large, compared to the radius of the components, such that the impact dynamics are not influenced by solar tides. However, this approximation is not necessarily true for moonlet impacts, especially if the impact occurs close to the planet. Therefore, moonlet impacts can be more erosive than planetary impacts as the velocity of ejected material required to reach the mutual Hill sphere is smaller than the gravitational escape velocity, altering the merger efficiency [Canup and Esposito, 1995].

Moonlet-moonlet collisions may be relevant for other satellite systems, for example, in the Neptunian system, where typical impact velocities between Triton and a primordial satellite system are expected to be high [Rufu and Canup, 2017], however, the impacts occur farther away from the planet, where tidal effects are minimal. In the Saturnian system, collisions among small and close-in satellites, could have created their peculiar shapes [Leleu et al., 2018]. Moreover, collision among satellites or within a potential well may be important for KBO objects as well. For example, in the formation of Haumea’s system (consisting of two satellites, collisional family members, Brown et al. 2007, and a newly observed ring, Ortiz et al. 2017) by a collision from an unbound KBO onto a pre-existing satellite [Schlichting and Sari, 2009]. For this system it has been proposed that the same impact is able to disrupt the satellite, form the current two companions and probably the ring [Schlichting and Sari, 2009].

In this work we estimate the merger efficiency of impacts within the planetary gravitational potential, where tidal forces alter the amount of mass that comprises the final moon. In order to directly compare our results with the standard impacts of two bodies in free space, we perform reference simulations with no central potential.

Previous simulations show that protolunar debris disks and their accreted moonlets have different isotopic signatures, depending on the parameters of the collision with the planet and the impactor’s isotopic signature [Rufu et al., 2017]. Moreover, in the single giant impact scenario, although moonlets are formed from the same debris disk, the moonlets are not sourced from the same regions in the debris disk. Material from the inner debris disk (inside the Roche limit), comprising most of the secondary moonlet, may experience some equilibration with the proto-Earth [Pahlevan and Stevenson, 2007; Salmon and Canup, 2012, 2014], therefore isotopic signatures between the two moonlets may still arise. After the merger of the two moonlets, the surface solidified in the the first 1000 yr, forming a conductive lid and prolonging the complete lunar solidification to ~ 10 Myr [Elkins-Tanton et al., 2011]. Therefore, the surface records the oldest stages of the lunar thermal evolution. Efficient post-impact convection, sub-

sequent impacts and/or subsequent melting due to tidal heating [Meyer et al., 2010], could disrupt the initial crust, but some initial heterogeneities may still be preserved on older terrains, such as, the lunar farside. In this study, we estimate the resulting initial surface mixing between moonlets after their merger, in order to test whether initial lunar crustal heterogeneities could emerge from the last global accretionary event [Robinson et al., 2016] and estimate whether future observed heterogeneities in lunar samples could distinguish between lunar origin scenarios (single vs. multiple moonlets).

Anorthositic material is widely observed on old lunar terrains and considered to represent the primordial lunar crust, formed from the flotation of plagioclase minerals from the lunar magma ocean (Elkins-Tanton et al. 2011; current crystallization studies require a depth of ~ 500 km to explain the observed lunar crustal thickness; Zuber et al. 2013; Charlier et al. 2018). An impact that occurs after the formation of the anorthositic crust (less than 1000 yr; Elkins-Tanton et al. 2011) can cause massive resurfacing, disrupting the previous anorthositic crust. Therefore, the amount of melt that is generated from moonlet impacts is important in order to assess whether an anorthositic global crust could reform from the secondary magma ocean phase.

In this work we perform hydrodynamic simulations of impacting moonlets within a planetary potential (described in section 2) to assess: (1) the merger efficiencies and to compare them to impacts of bodies in free space (section 3.1); (2) the initial surface mixing between the two moonlets (section 3.2); (3) the amount of melt that occurs during these impacts (section 3.3).

2 Methods

We perform Smoothed Particle Hydrodynamic (SPH) impact simulations of two orbiting moonlets, using GADGET2 [Springel, 2005] with a tabulated M-ANEOS equation of state for forsterite [Melosh, 2007] and ANEOS for iron [Thompson, 1990] (code modifications were performed by Marcus et al. 2009; Marcus 2011 and available in the supplemental material of Čuk and Stewart 2012). In this implementation material strength is not introduced as previous studies of impacts with lunar-sized bodies did not find significant differences when adding material forces [Jutzi and Asphaug, 2011]. Note that recent work suggests that material strength effects can increase the required energy to disrupt the body, particularly for small masses [Jutzi, 2015]. However, the expected impacting velocities in this scenario [Citron et al., 2018] are lower than the catastrophic disruption threshold. For planetary scale impacts, material strength was shown to more effectively disperse the heating in the mantle induced by the impact shock [Emsenhuber et al., 2018], therefore purely hydrodynamic simulation may underestimate the initial amount of melting in the mantle. Further studies are required in order to estimate the effect of material strength on the initial melt distribution and later stage deformation. While the exact role of material strength is somewhat unknown, we expect it to have a minimal effect on the impact results in this study, especially in regards to the final moonlet mass.

The impacting material consists of $\sim 2 \times 10^5$ particles while the planet is simulated using a small number of particles ($\sim 10^4$). The small planetary resolution efficiently represents the gravitational potential, however discontinuities in the hydrodynamic calculation could emerge if particles with distinctly different masses, as is the case for planetary and impacting material, are in close vicinity. In this current setup, these two types of particles rarely interact directly.

As the cores of the colliding bodies may erode during impact, we assume that the colliding bodies have 10% iron material, similar to the current upper estimate for the lunar iron fraction [Wood, 1986; Canup, 2004b]. To cover the range of possible Moon

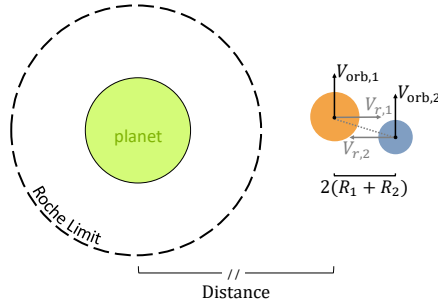


Figure 1. Schematic of the initial setup of the simulations. Each moonlet is given a circular orbital velocity ($V_{\text{orb},i}$) with an additional radial velocity component ($V_{r,i}$). The black dashed line represents the Roche limit of the planet. Sizes and distances are not to scale..

formation scenarios, we tested two extreme cases of initial thermal states, "cold" and "hot" (from previous studies of lunar evolution, *Laneuville et al.* 2013, see Text S1 in Supplementary material). Small differences were observed between the outcomes of the two states (see Figure S3 and S5 in Supplementary material), therefore the following results assume a "cold" initial thermal state. The bodies are simulated in isolation for 10 hours to allow their initial relaxation and to establish gravitational equilibrium. The temperature is then corrected to the initial thermal profile and simulated in isolation again for 10 hours for further relaxation. We verify this configuration is stable by ensuring that the RMS velocity of the particles is $< 1\%$ of the typical impact velocity, ~ 1 km/s.

The moonlets are placed on a orbit around an Earth-mass planet (M_{\oplus}) at three given distances ($1.5, 3, 5 R_{\text{Roche}}$, where $R_{\text{Roche}} = 18,381$ km is Earth's fluid Roche limit). The smaller distance represents a collision of two moonlets that are formed from the same debris disk and will impact early in their evolution [*Canup et al.*, 1999; *Jutzi and Asphaug*, 2011]. The larger distances represent the collision of two moonlets that are formed in different debris disks, as predicted by the multiple impact hypothesis. These impacts will occur farther away from the planet as the moonlets experienced some tidal evolution before impact [*Citron et al.*, 2018]. The moonlets are placed at $2(R_1 + R_2)$ (where R_i is the radius of moonlet i) distance from each other at the start of the simulation in order to allow for tidal forces to change the shape of the moonlets prior to impact (see Figure 1). We vary the mass ratio of the impacting moonlets ($\gamma = M_2/M_{\text{tot}}$, where M_2 is the smaller body and M_{tot} is the total impacting mass). In this work we choose to focus on the last impact that formed the Moon, hence the total impacting mass is constant and equal to one lunar mass ($M_{\text{tot}} = 1M_{\text{moon}}$). Initially, each moonlet is given a circular orbital velocity ($V_{\text{orb},i}$) with an additional radial velocity component ($V_{r,i}$), such that the radial velocity of the center of mass of the moonlets is zero. The maximum allowed impact velocity is the maximum radial velocity that maintains each moonlet on closed orbit around the planet with a perigee larger than the Roche limit, R_{Roche} , therefore, for smaller mass ratios or for larger planetary distance the maximum allowed velocity decreases. Because the moonlets move slightly around the planet before the impact (and the exact moment of impact is not recorded by the SPH output), we numerically estimate the impact angle and velocity by evolving the two moonlets until contact is established (by computing the 3-body gravitational interactions), assuming the bodies retain their spherical shape.

The simulations cover 48 hours of simulated time after impact. In some cases where the resulting moons did not reach a stable state, the simulations are continued for an additional 24 hours. It should be noted that for eccentric moonlets with perigees close to Roche limit or moonlets that continue to pass through a debris disk, the shape and surface of the moonlet will constantly change and equilibrium cannot be reached. The realistic simulated time is limited to a few days due to artificial viscosity that is introduced in the SPH code in order to mimic shock dissipation [Canup, 2004b].

At the end of the simulation, we use K-means clustering machine learning algorithm [Spath, 1985] to divide the mass into two clusters and obtain an initial guess on the mass and radius of the largest cluster. Subsequently, we use an iterative algorithm to find the bounded mass to that specific cluster. The algorithm uses the initial guess and classifies particles as bounded to the moonlet if they are within the Hill radius of the moonlet ($r_i < R_{\text{Hill},i}$, where r_i is the distance of the particle to moonlet i , $R_{\text{Hill},i} = a_i(M_i/3(M_{\oplus} + M_i))^{1/3}$ is the Hill radius of moonlet i and a_i its semimajor axis) and have a velocity smaller than that required to reach the Hill sphere of the moonlet [Bierhaus et al., 2012; Alvarelos, 2002]:

$$V_{\text{Hill}}^2 = \frac{2GM_i}{r_i} \left(\frac{R_{\text{Hill},i}^2 - R_{\text{Hill},i} \cdot r_i}{R_{\text{Hill},i}^2 - r_i^2 \sin^2 \zeta_i} \right) \quad (1)$$

where G is the gravitational constant, M_i is the mass of the moonlet i , and ζ is the angle of the particle relative to the moonlet (following Bierhaus et al., 2012, we assume that $\sin^2 \zeta \approx 0.5$). The moonlet's mass, Hill radius, and center of mass are adjusted and bounded particles are recalculated until convergence is achieved (typically a few iterations). Clustering algorithm is repeated on the material that is not bounded to the previously classified cluster, until the mass with high-density ($\rho > 1 \text{ g/cm}^3$) is smaller than $0.01 M_{\text{moon}}$ or the two most massive clusters have been classified.

In order to directly compare our results with the standard impacts of two bodies in free space we perform additional simulations with the same impact parameters but without a central potential. To insure that the angle and velocity of the impact at contact are equal to the previous set of simulations, we perform a backward integration (2-body interaction) from the moment of contact until a distance of 2 radii. We set these new positions and velocities as the new initial setup. We verified that the impact parameters in both cases (with/without central potential) are similar by comparing the positions and velocities of the moonlets at contact, as simulated by the hydrodynamic code. The resulting impact angle and velocity difference is $< 1^\circ$ and $< 0.001 V_{\text{esc}}$, respectively (where the mutual escape velocity is defined as $V_{\text{esc}} = \sqrt{2G(M_1 + M_2)/(R_1 + R_2)}$).

3 Results

3.1 Merger Efficiency

Previous works of ring material accretion near the Roche zone emphasized the difference between the accretion under the influence of tidal forces and accretion of material far from a central potential [Canup and Esposito, 1995]. However, as these studies estimate the accretion rate of debris composed of many small components, they do not consider the effect of the angle for each impact, but rather average the accretion efficiency for all angles, or assume radial alignment of the components, which promotes accretion [Canup and Esposito, 1995]. Our results show the transitions between accretion and hit-and-run regime at different angles and velocities. Estimating when grazing impacts occur is important because the merger efficiencies in this region is low and interactions between grazing moonlets can destabilize them towards the Roche limit, where they will be disintegrated by tidal forces (Figure 2-a; *e.g.* simulations in the hit-and-run regime with high angles and velocities above $1.4 V_{\text{esc}}$).

Importantly, in a tidal environment, the boundary of the hit-and-run regime is expanded and such impacts are more abundant. For example, the low angle and high velocity impact in Figure 2-a resulted in two large remnants (largest remnant mass, $M_{\text{lr}} = 0.28 M_{\text{tot}}$; second largest remnant mass, $M_{\text{sr}} = 0.27 M_{\text{tot}}$). This impact is below the grazing curve [Genda *et al.*, 2012], therefore a single final body was expected. We confirmed this disparity by simulating the same impact in free space, which resulted in a single final body of mass $0.71 M_{\text{tot}}$ (Figure 2-c). In both cases the bodies graze after the first impact. In the case with the central potential, the bodies expand beyond the mutual Hill radius (dashed lines in Figure 3-a) and gravitationally separate, as opposed to the free space case where the bodies do not have enough energy to escape the mutual gravitational pull and re-impact again after 5 hours (Figure 3-b). Overall, the transition to the hit-and-run regime occurs at a lower velocity when the impact occurs closer to the planet (Figure 4-a). The Hill escape velocity (Eq. 1, here we defined R_{Hill} as the mutual Hill radius of both impacting moons and set $r = R_1 + R_2$) at $1.5 R_{\text{Roche}}$ is $\sim 0.7 V_{\text{esc}}$, whereas at $5.0 R_{\text{Roche}}$ it is $\sim 0.9 V_{\text{esc}}$. By normalizing the impact velocity to the local Hill escape velocity, V_{Hill} , rather than the escape velocity [Genda *et al.*, 2012], we find that the transition to the hit-and-run regime occurs at the same normalized velocity (Figure 4-b).

Citron *et al.* [2018] found that most impacts are at a velocity $< 1.75 V_{\text{esc}}$, and these will have a high merger efficiency if the impact angle is low enough for accretion, but these also include hit-and-run impacts for higher angles. Because grazing angles are the most probable ($\sim 45^\circ$), most similar size impacts will usually not accrete at velocities $> V_{\text{esc}}$. Hit-and-run impacts transfer little angular momentum between the orbiting components. Therefore, moonlets will remain on approximately similar orbits, and will likely impact several times [Asphaug, 2010] until the final accretion or the loss of one moonlet (*e.g.*, Supplemental Movie S1). Perfect merger is often assumed in dynamical studies [Kokubo *et al.*, 2006; Raymond *et al.*, 2009; Rufu and Canup, 2017; Citron *et al.*, 2018], however resolving hit-and-run impacts is important, as each impact can raise the melting fraction of the final moon (see section 3.3) and could potentially dynamically destabilize moonlets (as is the case for the impacts near the Roche limit).

For impacts in free space and small impacting angles, partial accretion is expected (Figure 2 - light blue region; most of the impacting mass should be retained within a single body). Previous studies found that the mass of the largest remnant in accretionary impacts, M_{lr} , is linearly proportional to the kinetic energy of the impact, Q_R ,

$$M_{\text{lr}}/M_{\text{tot}} \propto -Q_R/Q'_{RD} \quad (2)$$

where, Q'_{RD} , is defined as the disruptive (catastrophic) energy required for $M_{\text{lr}} = 0.5 M_{\text{tot}}$ [Stewart and Leinhardt, 2009]. However, for impacts within a central potential, we observe that with decreasing planetary distance, debris generation is enhanced because the Hill radius of the orbiting moonlet is smaller. Hence, ejected material requires less energy to escape the gravitational pull of the moonlet (Eq. 1) and typical merger efficiencies are lower (light blue line in Figure 5-a) than predicted from previously defined scaling laws in free space (red line in Figure 5-a; Leinhardt and Stewart, 2012). The disruptive energy scales as, $Q'_{RD} \propto V^{*2-3\bar{\mu}}$, where $\bar{\mu}$ is a dimensionless material constant [Housen and Holsapple, 1990; Leinhardt and Stewart, 2012], and V^* is the catastrophic velocity and proportional to the escape velocity, $V^* \propto V_{\text{esc}}$. Hence, the scaling between the catastrophic energy in free space scales to the escape velocity as, $Q'_{RD} \propto V_{\text{esc}}^{2-3\bar{\mu}}$. Similarly, for impacts within a central potential we scale the disruptive energy to the velocity required to escape from the Hill sphere (rather the mutual escape velocity) hence:

$$Q'_{RD,\text{Hill}} = Q'_{RD} (V_{\text{Hill}}/V_{\text{esc}})^{2-3\bar{\mu}} \quad (3)$$

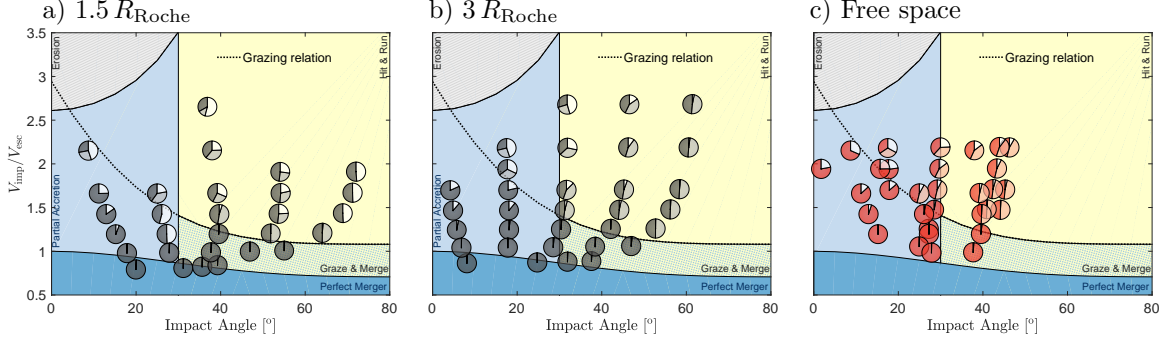


Figure 2. Merger efficiencies for impacts between two half-moon-sized bodies in angle-velocity phase space. Impacts occurred at a distance of a) $1.5 R_{\text{Roche}}$; b) $3 R_{\text{Roche}}$ from the planet; for comparison, c) impacts of two bodies in free space (no central potential). Each pie plot represents the distribution of the final impacting mass (the largest remnant - dark gray/red; if present the second largest remnant - light gray/red; debris material - white). The different regions of the plot represent different impacting regimes previously defined by *Leinhardt and Stewart* [2012] for two bodies in free space (with the best fitted parameter of energy dissipation within the target, $c^*=2.8$). The dashed line represents the critical velocity for which grazing occurs, previously defined by *Genda et al.* [2012].

We find that with the corrected disrupting energy, one slope fits well with the results from different planetary distances (Figure 5-b).

Overall, in both grazing and non-grazing cases, the merger efficiency is lower near the Roche limit and erosion of the moonlet is enhanced. The generated debris typically remain in orbit and can reaccrete on the surface of the surviving moonlet or fall onto the planet.

3.2 Surface Properties

Different moonlets can inherit different isotopic compositions, either because each moonlet is sourced from a distinct region in the heterogeneous debris disk [*Salmon and Canup*, 2012], or because each moonlet is accreted from a distinct debris disk generated by different impacts [*Rufu et al.*, 2017]. In order to estimate the initial surface heterogeneities in the moon after the last global impact event, we checked whether large areas containing contributions from a single moonlet exist on the surface. Our motivation being that, if surface heterogeneities are present, they could be preserved only in the upper layer, as it quickly solidifies.

For each particle at the surface (material in the upper 5% layer in the volume enclosed by a longitude-latitude rectangle of $15^\circ \times 15^\circ$, and typically represented by ~ 1000 particles; see Text S2 for other definitions) of the surviving moonlet we calculate $f_{\text{moon}1} - f_{\text{moon}2}$ (where $f_{\text{moon},i}$ is the fraction of surface particles in the neighborhood sourced from moon i). The width defining the surface layer is chosen as it samples the upper 80 km layer, therefore only large subsequent impacts (of the order of the South-Pole Aitken-forming impact, *Melosh et al.* 2017) could drastically disrupt this layer and excavate enough material to bury these signatures. SPH lacks the ability to resolve the small scales required for chemical equilibration, therefore, the length defining each neighbourhood is 400 km, ensuring that only large scale heterogeneities are resolved (typically resulting in ~ 100 neighbours for each particle; see Text S2 for sensitivity analysis on this value). Moreover, we emphasize that this is an estimation

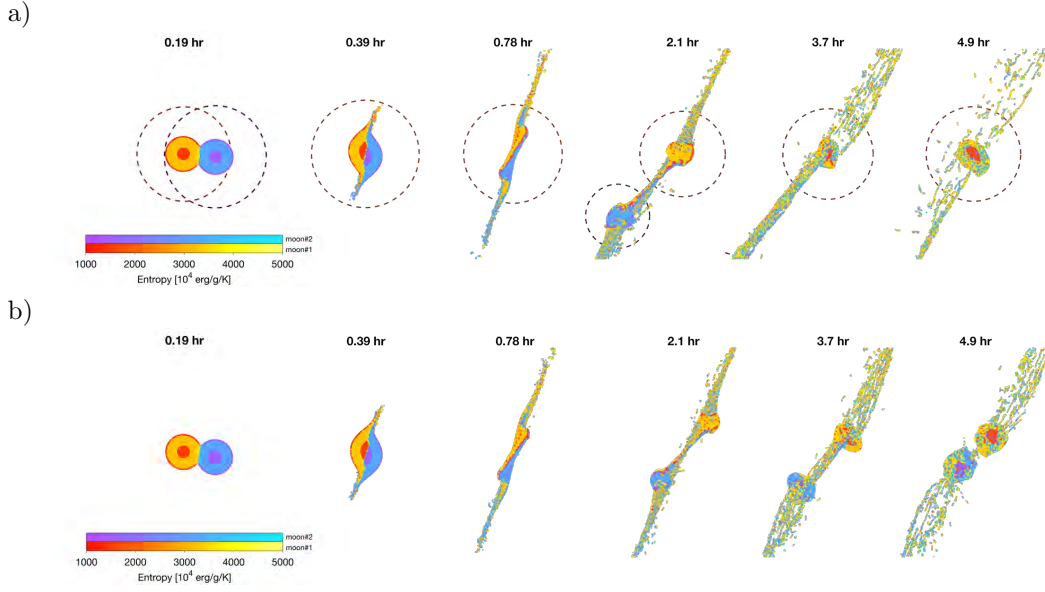


Figure 3. Differences between impact with and without the central potential. Several snapshots with similar initial conditions ($\beta = 8.75^\circ$; $V_{\text{imp}} = 2.15 V_{\text{esc}}$) of a) two orbiting moonlets inside the planetary gravitational potential; b) two bodies in free space. The different color bars represent the entropy of the material originating from different moonlets. All projections are on the equatorial plane with one hemisphere removed. The Hill sphere of each orbiting moonlet is represented by the dashed lines. For simplicity, only material with density of $\rho > 3 \text{ [g/cm}^3\text{]}$ is shown.

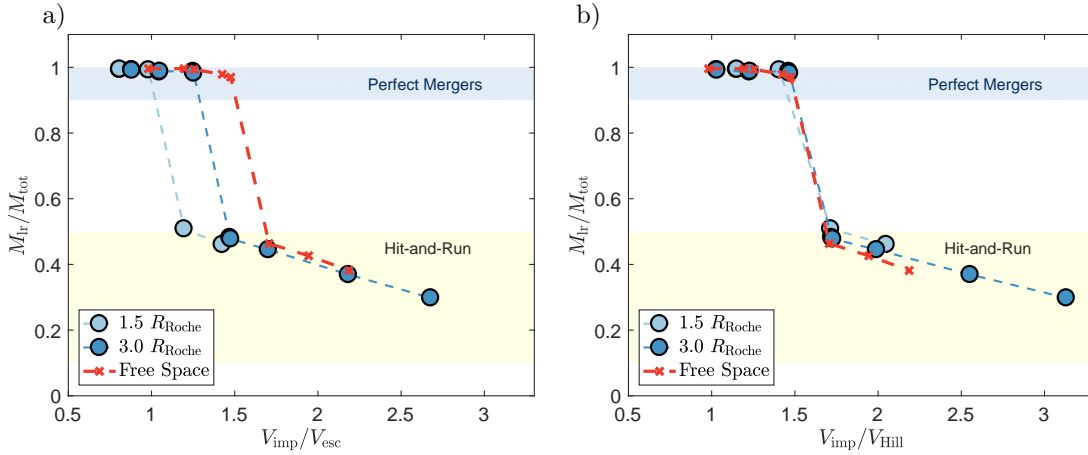


Figure 4. Transition to hit-and-run regime. Normalized mass of largest remnant vs. impact velocity normalized by the a) mutual escape velocity; b) Hill escape velocity (for free space cases we set $V_{\text{Hill}} = V_{\text{esc}}$) for impact angle of $\beta \sim 30^\circ$. Circled markers represent moonlet impacts at different distances from the planet whereas the crosses represent impacts of two bodies in free space (no central potential).

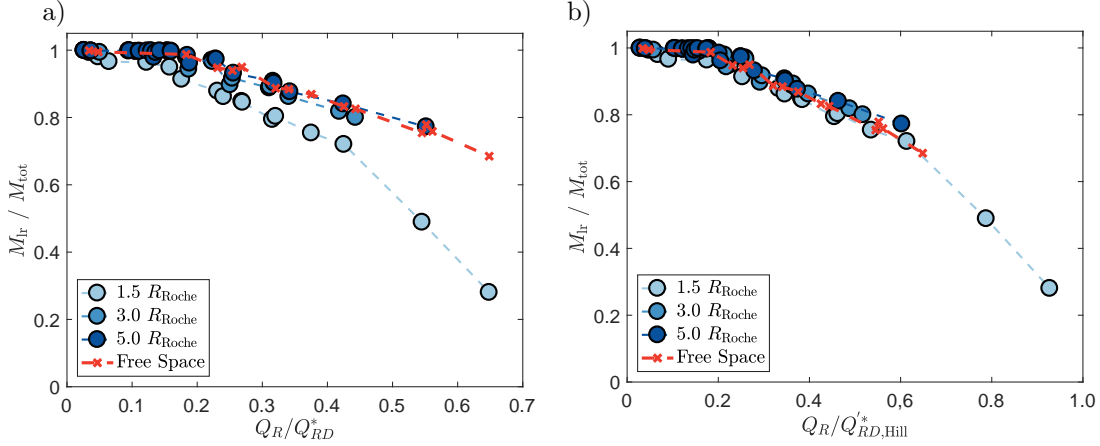


Figure 5. Mass of largest remnant post impact for low impact angles. Normalized mass of largest remnant vs. normalized impact energy for low impact angles ($\beta < 15^\circ$). The impact energy is normalized by a) the catastrophic disruption criteria Q'_{RD} , defined by *Leinhardt and Stewart* (2012; with the best fitted parameter of energy dissipation within the target, $c^* = 2.8$); b) the corrected Hill catastrophic disruption criteria, $Q'_{RD,Hill} = Q'_{RD}(V_{Hill}/V_{esc})^{2-3\bar{\mu}}$ (where $\bar{\mu} = 0.36$ is a dimensionless material constant [*Housen and Holsapple, 1990; Leinhardt and Stewart, 2012*]; for free space cases we set $V_{Hill} = V_{esc}$). Circle markers represent impacts at different distances from the planet whereas the crosses represent impacts of two bodies in free space (no central potential)

of the immediate post-impact surface variation, and additional post-impact process (*e.g.*, resurfacing due to impacts, vigorous convection or small scale instabilities) could remix the surface and remove any prior variations. However, the motivation of this study is to estimate an upper limit on the heterogeneities emerging from the last global event.

The resulted surface patterns show that low velocity and head-on impacts do not efficiently mix the surface of the resulting product because differential rotation post impact is limited. In these rare cases, large surface heterogeneities occur (Figure 6-a, e). More typical accretionary impacts of comparable-sized components have a larger amount of mixing (Figure 6-b, f). Specifically, surface variations for smaller mass ratios is decreased by the disruption of the small body and the reaccretion of material on the surface of the surviving moonlet (Figure 6-f, h; with similar initial condition and findings of *Jutzi and Asphaug 2011*). In hit-and-runs impacts, which are more probable for larger mass ratios, little mass is transferred by the impact, therefore, only small-scale heterogeneities are created (Figure 6-c, g). However, because the large components usually survive intact after impact, subsequent impacts could transfer additional material to the surface, creating a surface that is sourced almost equally from both moonlets (Figure 6-d).

It should be noted that for the highly erosive impacts or cases where one moonlet is disrupted due to passage through the planetary Roche limit, large amount of debris is generated and reaccreted on the surface of the surviving moonlet. The reaccretion timescale is larger than computationally attainable with SPH methods. Therefore, in these cases, we expect the overall surface variation to decrease, supporting our conclusions that typically surfaces are mixed.

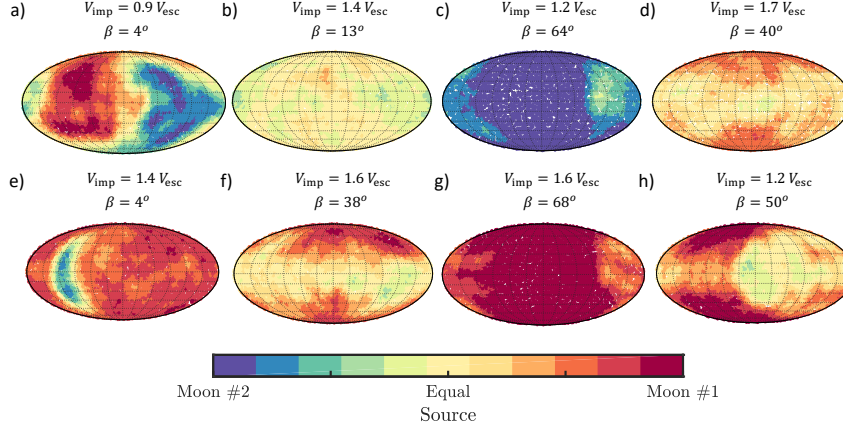


Figure 6. Examples of source material distribution on surfaces resulting from impacts between components with different mass ratios, $\gamma=0.5$ (first row) and $\gamma=0.1$ (second row). The velocity (V_{imp}) and impact angle (β) are denoted above each panel. The examples span the different regions of impact outcome: a)/e) low impact angle resulting in a perfect merger; b)/f) partial accretion; c)/g) single hit-and-run impact; d) sequence of two hit-and-run impacts; h) disruption and reaccretion of the smaller component on the larger component.

3.3 Melting

The highland terrain comprises about 77% of the lunar surface area and is composed mostly of anorthositic material [Taylor and Wieczorek, 2014]. Anorthosites are rarely present in the Procellarum KREEP terrane and remote sensing identified anorthosites only in the outer edges of the South Pole Aitken Basin [Taylor and Wieczorek, 2014]. Anorthositic-poor regions, comprising 23% of the lunar area, are correlated with younger surfaces, therefore the anorthositic materials are considered to represent the initial crust. The leading theory of the formation of the anorthositic crust is the flotation of plagioclase minerals from a lunar magma ocean [Elkins-Tanton *et al.*, 2011]. Gravity data from GRAIL [Zuber *et al.*, 2013] reveal igneous intrusions that provide evidence for a lunar radial expansion and consistent with a solidification of a 200-300 km-deep magma ocean [Andrews-Hanna *et al.*, 2013]. However, recent lunar crystallization studies [Charlier *et al.*, 2018] reveal that magma ocean of ~ 500 km is required to explain the lunar crustal thickness observed by GRAIL. Moreover, deeper magma oceans are possible if plagioclase flotation is imperfect or trapped liquids in cumulates are considered. Due to the uncertainties on the magma ocean depth required to reconcile the observations (crust thickness and lunar expansion limits), and the uncertainties on the initial thermal state of the moonlets, we estimate that a magma ocean depth > 200 km resulting from a "cold" initial thermal state is compatible with recrystallizing a global anorthositic crust.

We consider that material melted if the final entropy of the particle is larger than the value defined by the liquidus curve (calculated using the M-ANEOS code, Melosh, 2007; see Figure S4 in Supplementary material) at that density. We assume a "cold" thermal initial state and ignore partially melted material, therefore this is a lower boundary for the total amount of melt after impact (see Figure S5 in Supplementary material for differences between the two thermal states).

Because the impact velocities are small (~ 1 km/s), melting induced by shock heating in early stages of the impact is limited. However, interactions of bodies of comparable size lead to greater mantle-redistribution. This in turn promotes melt-

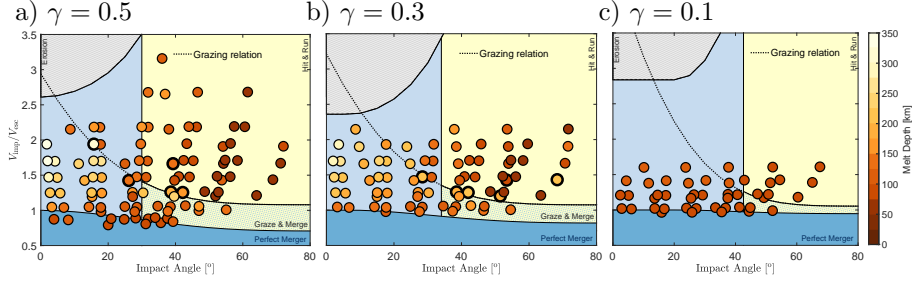


Figure 7. Depth of magma ocean in the angle-velocity phase space. Impacts between components with different mass ratios, a) $\gamma = 0.5$; b) $\gamma = 0.3$; c) $\gamma = 0.1$. Colors represent the overall magma-ocean-depth, assuming that the melt is homogeneously distributed on the top layers of the moonlet. The different regions of the plot represent different impacting regimes previously defined by *Leinhardt and Stewart* [2012] for two bodies in free space (with the best fitted parameter of energy dissipation within the target, $c^*=2.8$). The dashed line represents the critical velocity for which grazing occurs, previously defined by *Genda et al.* [2012]. The bullets with the black thick line represent simulations where the bodies impact twice, therefore, in these cases the magma ocean depth is higher.

ing by decompression, shear heating, and gravitational energy release from infalling material. High energy accretionary impacts can melt about 40% of the final moon’s mantle, corresponding to ~ 300 km-deep magma ocean (assuming that all the melt is concentrated on the top layers of the moon; Figure 7). On the other hand, hit-and-run impacts will result in less than $< 10\%$ melt, corresponding to < 100 km-deep magma ocean. As discussed before, in the non-disruptive hit-and-run cases, we expect that components will impact again as they remain on intersecting orbits after the first impact. The reimpacting timescale is shorter (a few orbits \sim hours – days) than the crust formation timescale (1000 yr; *Elkins-Tanton et al.* 2011). Therefore, sequences of impacts (*e.g.* two hit-and-run impacts, Figure 8, and a hit-and-run followed by an accretionary impact, Figure 9) add additional melt to the mantle of the surviving moonlet. Sequences of hit-and-run impacts do not transfer substantial mass between the impacts, but they can provide an additional heating source to the lunar magma ocean.

For accretionary impacts with high mass ratios, a magma ocean of > 200 km is expected, which is consistent with the required magma ocean depth to form the lunar crust [*Andrews-Hanna et al.*, 2013]. For impacts with small mass ratios, melt production is not efficient because these impacts are not energetic enough to disrupt and melt the body.

3.4 Discussion and Conclusions

We tested impacts between two orbiting moonlets. The classical phase space of two bodies in free space [*Leinhardt and Stewart*, 2012] is altered when the impacts occur under the influence of a planetary potential. For comparable-sized impactors, hit-and-run impacts (bodies graze and transfer little amount of material) prevail over accretionary impacts [*Asphaug*, 2010]. This abundance is further increased in the tidal environment, as Hill spheres are smaller with decreasing distance to the planet and impacting bodies will require less energy to reach the point where they are not gravitationally bound. Similarly, erosion is increased in the tidal environment and the energy required for disruption (estimated by previous works, *e.g.* *Movshovitz et al.* 2016) is smaller. Interactions between grazing moonlets can destabilize moonlets towards the

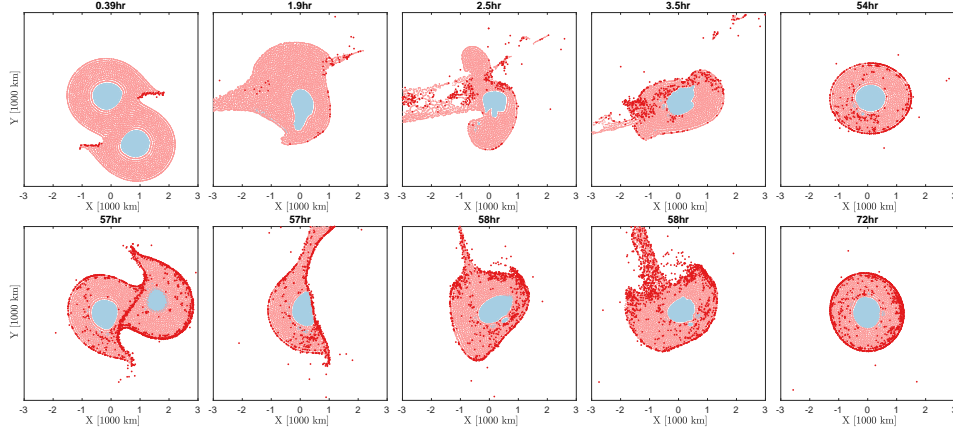


Figure 8. Melt evolution of a sequence of two hit-and-run impacts. Snapshots of two colliding half moonlets at a distance of $1.5 R_{\text{Roche}}$ from the planet (first impact: $\beta = 40^\circ$; $V_{\text{imp}} = 1.66 V_{\text{esc}}$; second impact: $\beta = 44^\circ$; $V_{\text{imp}} = 1.56 V_{\text{esc}}$). The snapshots show a slice of width 100 km centered in the equatorial plane of the surviving moon. The blue particles represent iron material and light/dark red particles represent the unmelted/melted magma material. Note that for emphasizing purposes, the melted particles are larger. In the first (first row) and second impact (second row), melt is created mainly in the secondary stage of the impact, where material falls back to the surface. Full movie can be found in the Supplementary material (Movie S2).

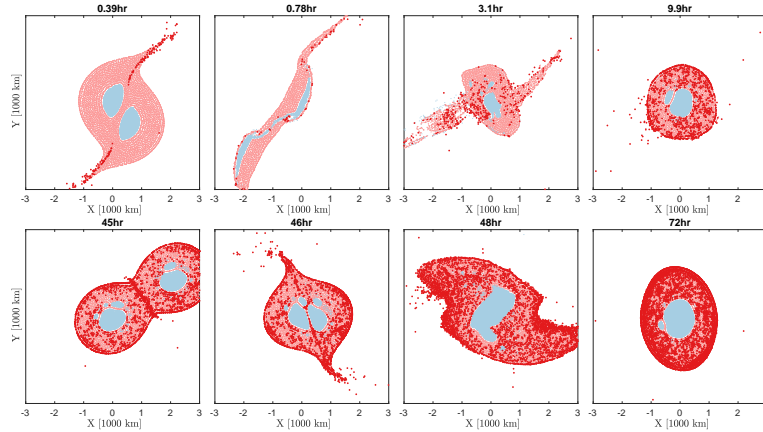


Figure 9. Melt evolution of a hit-and-run impact followed by accretory impact. Sequence of snapshots from two colliding half moonlets at a distance of $5 R_{\text{Roche}}$ from the planet (first impact: $\beta = 15^\circ$, $V_{\text{imp}} = 1.94 V_{\text{esc}}$; second impact: $\beta = 10^\circ$, $V_{\text{imp}} = 0.87 V_{\text{esc}}$). The snapshots show a slice of width 100 km centered in the equatorial plane of the surviving moon. Note that for emphasizing purposes, the melted particles are larger. The blue particles represent iron material and light/dark red particles represent the unmelted/melted magma material. In the first hit-and-run impact (first row), melt is mostly created in the secondary stage of the impact, where material falls back to the surface. In the second accretory impact (second row), melt is mostly created during the deformation and redistribution of material.

Roche limit, where they will be disintegrated by tidal forces. The produced debris remain in orbit and can later accrete by the surviving moon, enhancing the surface mixing, or fall onto the planet. Additionally, generated debris disks can reform moonlets, similar to the scenario proposed by *Hesselbrock and Minton* [2017] for the formation of the Martian satellites. Overall, we find that moonlet merger efficiencies are lower than previously estimated by free-space simulations, therefore, dynamical studies of the evolution of multiple satellite should include some degree of fragmentation.

Overall, if the last two components of the final Moon are comparable in size, mixing between the colliding bodies is efficient, and surface heterogeneities are not likely. We note that these results represent the immediate post-impact surface variation, and emphasize that additional post-impact processes would decrease prior surface variations, further supporting our conclusions that surfaces resulting from the last-global-accretionary events are well mixed. The amount of mixing can be probed by future lunar samples (*e.g.*, *Chang'e 5* sample return mission) and compared with previously observed heterogeneities [*Robinson and Taylor*, 2014; *Robinson et al.*, 2016]. Unfortunately, the lack of future observed heterogeneities could not preferentiate between scenarios with single or multiple moonlets impact, as the initial mixing efficiency is high.

We estimated the typical amount of melting in moonlet impacts and their contribution to the lunar magma ocean. Overall, impacts of comparable-sized components can melt significant portions of the mantle, mainly due to redistribution of material. A smaller contribution occurs in the early stages of the impact, when shock heating is important. The observed anorthositic crust, which is created fast, after the solidification of $\sim 80\%$ of the magma ocean [*Elkins-Tanton et al.*, 2011] could reform after the merging impact. The impacts between moonlets extend the magma ocean phase of the final Moon. Additionally, our results show that the majority of small-sized impactors are not energetic enough to disrupt the moonlet and hence do not create enough melt to account for the observed anorthositic crust. Therefore, to avoid the disruption of the observed anorthositic lunar crust, impacts of smaller size components can occur only early in the evolution (less than 1000 yr; *Elkins-Tanton et al.* 2011) before crustal disruption is recorded. After crustal formation, resurfacing due to subsequent impacts is limited. We therefore conclude that in the context of the moonlet merger scenario, a relatively large last event is preferred in order to account for the global distribution of a floatation crust [*Taylor and Wieczorek*, 2014].

Acknowledgments

We thank Dave Stevenson for helpful discussions. This project was supported by the Helen Kimmel Center for Planetary Science, the Minerva Center for Life Under Extreme Planetary Conditions, and by the I-CORE Program of the PBC and ISF (Center No. 1829/12). R.R. is grateful to the Israel Ministry of Science, Technology and Space for their Shulamit Aloni fellowship and NASA's SSERVI program for support. We thank Simon Lock and an anonymous reviewer for their thoughtful comments and suggestions that improved the final version of this manuscript. The modified version of GADGET-2 and EOS tables are available in the supporting information of *Čuk and Stewart* [2012]. A summary of the impact results is included in the supplementary material.

References

Alvarellos, J. (2002), Orbital evolution of impact ejecta from Ganymede, *Icarus*, 160(1), 108–123.

- Andrews-Hanna, J. C., S. W. Asmar, J. W. Head, W. S. Kiefer, A. S. Konopliv, F. G. Lemoine, I. Matsuyama, E. Mazarico, P. J. McGovern, H. J. Melosh, et al. (2013), Ancient igneous intrusions and early expansion of the Moon revealed by GRAIL gravity gradiometry, *Science*, *339*(6120), 675–678.
- Asphaug, E. (2010), Similar-sized collisions and the diversity of planets, *Chemie der Erde-Geochemistry*, *70*(3), 199–219.
- Benz, W., A. Cameron, and H. Melosh (1989), The origin of the Moon and the single-impact hypothesis III, *Icarus*, *81*(1), 113 – 131.
- Bierhaus, E. B., L. Dones, J. L. Alvarillos, and K. Zahnle (2012), The role of ejecta in the small crater populations on the mid-sized Saturnian satellites, *Icarus*, *218*(1), 602–621.
- Brown, M. E., K. M. Barkume, D. Ragozzine, and E. L. Schaller (2007), A collisional family of icy objects in the Kuiper belt, *Nature*, *446*(7133), 294–296.
- Cameron, A. G., and W. R. Ward (1976), The origin of the Moon, in *Lunar and Planetary Science Conference*, vol. 7.
- Canup, R. (2005), A giant impact origin of Pluto-Charon, *Science*, *307*(5709), 546–550.
- Canup, R. M. (2004a), Dynamics of lunar formation, *Annual Review of Astronomy and Astrophysics*, *42*(1), 441–475.
- Canup, R. M. (2004b), Simulations of a late lunar-forming impact, *Icarus*, *168*(2), 433–456.
- Canup, R. M. (2008), Lunar-forming collisions with pre-impact rotation, *Icarus*, *196*(2), 518–538.
- Canup, R. M. (2012), Forming a Moon with an Earth-like composition via a giant impact, *Science*, *338*(6110), 1052–1055.
- Canup, R. M., and E. Asphaug (2001), Origin of the Moon in a giant impact near the end of the Earth’s formation, *Nature*, *412*(6848), 708.
- Canup, R. M., and L. W. Esposito (1995), Accretion in the Roche zone: Coexistence of rings and ringmoons, *Icarus*, *113*(2), 331–352.
- Canup, R. M., H. F. Levison, and G. R. Stewart (1999), Evolution of a terrestrial multiple-moon system, *The Astronomical Journal*, *117*(1), 603.
- Charlier, B., T. L. Grove, O. Namur, and F. Holtz (2018), Crystallization of the lunar magma ocean and the primordial mantle-crust differentiation of the Moon, *Geochimica et Cosmochimica Acta*, *234*, 50–69.
- Citron, R. I., H. B. Perets, and O. Aharonson (2018), The role of multiple giant impacts in the formation of the Earth-Moon system, *The Astrophysical Journal*, *862*(1), 5.
- Ćuk, M., and S. T. Stewart (2012), Making the Moon from a fast-spinning Earth: A giant impact followed by resonant despinning, *Science*, *338*(6110), 1047–1052.
- Elkins-Tanton, L. T., S. Burgess, and Q.-Z. Yin (2011), The lunar magma ocean: Reconciling the solidification process with lunar petrology and geochronology, *Earth and Planetary Science Letters*, *304*(3), 326–336.
- Emsenhuber, A., M. Jutzi, and W. Benz (2018), SPH calculations of Mars-scale collisions: The role of the equation of state, material rheologies, and numerical effects, *Icarus*, *301*, 247–257.
- Genda, H., E. Kokubo, and S. Ida (2012), Merging criteria for giant impacts of protoplanets, *The Astrophysical Journal*, *744*(2), 137.
- Hartmann, W. K., and D. R. Davis (1975), Satellite-sized planetesimals and lunar origin, *Icarus*, *24*(4), 504–515.
- Hesselbrock, A. J., and D. A. Minton (2017), An ongoing satellite–ring cycle of Mars and the origins of Phobos and Deimos, *Nature Geoscience*, *10*(4), 266.
- Housen, K. R., and K. A. Holsapple (1990), On the fragmentation of asteroids and planetary satellites, *Icarus*, *84*(1), 226–253.
- Ida, S., R. M. Canup, and G. R. Stewart (1997), Lunar accretion from an impact-generated disk, *Nature*, *389*(6649), 353–357.

- Jutzi, M. (2015), SPH calculations of asteroid disruptions: The role of pressure dependent failure models, *Planetary and space science*, *107*, 3–9.
- Jutzi, M., and E. Asphaug (2011), Forming the lunar farside highlands by accretion of a companion moon, *Nature*, *476*(7358), 69–72.
- Kokubo, E., J. Kominami, and S. Ida (2006), Formation of terrestrial planets from protoplanets. I. Statistics of basic dynamical properties, *The Astrophysical Journal*, *642*(2), 1131.
- Laneuville, M., M. A. Wieczorek, D. Breuer, and N. Tosi (2013), Asymmetric thermal evolution of the Moon, *Journal of Geophysical Research: Planets*, *118*(7), 1435–1452.
- Leinhardt, Z. M., and S. T. Stewart (2012), Collisions between gravity-dominated bodies. I. Outcome regimes and scaling laws, *The Astrophysical Journal*, *745*(1), 79.
- Leleu, A., M. Jutzi, and M. Rubin (2018), The peculiar shapes of Saturn’s small inner moons as evidence of mergers of similar-sized moonlets, *Nature Astronomy*, *2*(7), 555–561.
- Lock, S. J., S. T. Stewart, M. I. Petaev, Z. Leinhardt, M. T. Mace, S. B. Jacobsen, and M. Cuk (2018), The origin of the Moon within a terrestrial synestia, *Journal of Geophysical Research: Planets*, *123*(4), 910–951.
- Marcus, R. A. (2011), *The role of giant impacts in planet formation and internal structure*, Harvard University.
- Marcus, R. A., S. T. Stewart, D. Sasselov, and L. Hernquist (2009), Collisional stripping and disruption of super-earths, *The Astrophysical Journal Letters*, *700*(2), L118.
- Melosh, H. (2007), A hydrocode equation of state for SiO₂, *Meteoritics & Planetary Science*, *42*(12), 2079–2098.
- Melosh, H., J. Kendall, B. Horgan, B. Johnson, T. Bowling, P. Lucey, and G. Taylor (2017), South Pole–Aitken basin ejecta reveal the Moon’s upper mantle, *Geology*, *45*(12), 1063–1066.
- Meyer, J., L. Elkins-Tanton, and J. Wisdom (2010), Coupled thermal–orbital evolution of the early Moon, *Icarus*, *208*(1), 1–10.
- Movshovitz, N., F. Nimmo, D. Korycansky, E. Asphaug, and J. Owen (2016), Impact disruption of gravity-dominated bodies: New simulation data and scaling, *Icarus*, *275*, 85 – 96.
- Ortiz, J. L., P. Santos-Sanz, B. Sicardy, G. Benedetti-Rossi, D. Bérard, N. Morales, R. Duffard, F. Braga-Ribas, U. Hopp, C. Ries, et al. (2017), The size, shape, density and ring of the dwarf planet Haumea from a stellar occultation, *Nature*, *550*(7675), 219.
- Pahlevan, K., and D. J. Stevenson (2007), Equilibration in the aftermath of the lunar-forming giant impact, *Earth and Planetary Science Letters*, *262*, 438–449.
- Raymond, S. N., D. P. O’Brien, A. Morbidelli, and N. A. Kaib (2009), Building the terrestrial planets: Constrained accretion in the inner solar system, *Icarus*, *203*(2), 644 – 662.
- Robinson, K. L., and G. J. Taylor (2014), Heterogeneous distribution of water in the Moon, *Nature Geoscience*, *7*(6), 401.
- Robinson, K. L., J. J. Barnes, K. Nagashima, A. Thomen, I. A. Franchi, G. R. Huss, M. Anand, and G. J. Taylor (2016), Water in evolved lunar rocks: Evidence for multiple reservoirs, *Geochimica et Cosmochimica Acta*, *188*, 244 – 260.
- Rufu, R., and R. M. Canup (2017), Triton’s evolution with a primordial Neptunian satellite system, *The Astronomical Journal*, *154*(5), 208.
- Rufu, R., O. Aharonson, and H. B. Perets (2017), A multiple-impact origin for the Moon, *Nature Geoscience*, *10*, 89 – 94.
- Salmon, J., and R. M. Canup (2012), Lunar accretion from a Roche-interior fluid disk, *The Astrophysical Journal*, *760*(1), 83.

- Salmon, J., and R. M. Canup (2014), Accretion of the Moon from non-canonical discs, *Philosophical Transactions of the Royal Society of London A: Mathematical, Physical and Engineering Sciences*, *372*(2024).
- Schlichting, H. E., and R. Sari (2009), The creation of Haumea’s collisional family, *The Astrophysical Journal*, *700*(2), 1242.
- Spath, H. (1985), *The cluster dissection and analysis theory fortran programs examples*, Prentice-Hall, Inc.
- Springel, V. (2005), The cosmological simulation code GADGET-2, *Monthly Notices of the Royal Astronomical Society*, *364*(4), 1105–1134, doi:10.1111/j.1365-2966.2005.09655.x.
- Stewart, S. T., and Z. M. Leinhardt (2009), Velocity-dependent catastrophic disruption criteria for planetesimals, *The Astrophysical Journal Letters*, *691*(2), L133.
- Taylor, G. J., and M. A. Wieczorek (2014), Lunar bulk chemical composition: a post-gravity recovery and interior laboratory reassessment, *Phil. Trans. R. Soc. A*, *372*(2024), 20130,242.
- Thompson, S. (1990), Aneos—analytic equations of state for shock physics codes, sandia natl, *Lab. Doc. SAND89-2951*.
- Wood, J. (1986), Moon over Mauna Loa - A review of hypotheses of formation of Earth’s Moon, in *Origin of the Moon*, edited by W. Hartmann, R. Phillips, and G. Taylor, pp. 17–55.
- Zuber, M. T., D. E. Smith, M. M. Watkins, S. W. Asmar, A. S. Konopliv, F. G. Lemoine, H. J. Melosh, G. A. Neumann, R. J. Phillips, S. C. Solomon, et al. (2013), Gravity field of the Moon from the gravity recovery and interior laboratory (GRAIL) mission, *Science*, *339*(6120), 668–671.

Supporting Information for “Impact Dynamics of Moons Inside a Planetary Potential”

R. Rufu^{1,2} and O. Aharonson^{1,3}

¹Weizmann Institute of Science, Department of Earth and Planetary Sciences, Rehovot, Israel

²Southwest Research Institute, 1050 Walnut Street, Suite 300, Boulder, CO 80302, USA

³Planetary Science Institute, Tucson, AZ, USA

Contents

1. Text S1 to S2
2. Figure S1 to S7
3. Caption Movie S1 to S2

Text S1 - Variations due to Different Initial Thermal States

Different lunar formation scenarios can predict different initial thermal states, depending on the exact masses and separation of the two moonlets, the impact timescale, and hence the cooling time before impact, may vary [Canup *et al.*, 1999]. For example, the canonical scenario [Canup, 2004] would predict a fully molten Moon [Barr, 2016], that would require 10 Myr for total solidification [Elkins-Tanton *et al.*, 2011]. Whereas, in the multiple impact hypothesis, the resulting moonlets are smaller (faster solidification) and the time between moonlet merger is longer, mostly depending on the moonlet formation timescale. To cover the range of possible Moon formation scenarios, we tested two extreme cases of initial thermal states, “cold” and “hot” states from previous studies (Laneville *et al.*, 2013; see Figure S1). For both initial states the surface temperature is set to 250 [K]. Although, we chose two extreme cases, still the maximum temperature difference between the two moonlets is 200 K, resulting in a maximum density (sound speed) difference of 0.02 g/cm³ (0.2 km/s). We performed 48 pairs of impact simulations between two comparable-size bodies with different impact parameters, spanning the regimes found in subsection 3.1.

In order to statistically quantify the surface variation in this sections, we choose to represent the overall surface variation as:

$$\Delta_{\text{surf}} = \sigma - \sigma_{\text{rand}} \quad (1)$$

where, σ is the standard variation of the surface particles values ($f_{\text{moon1}} - f_{\text{moon2}}$, as defined in section 3.2) and σ_{rand} is the standard variation of a random distribution of the surface particles. Under this definition, small values of Δ_{surf} are expected for surfaces that are well mixed between two bodies (Figure S2-a) or surfaces that include material from one moonlet (Figure S2-b). Whereas, large values of Δ_{surf} are expected for surfaces that include material from both bodies but their material is not mixed, creating regions where the material is unproportionally sourced (Figure S2-c, d). The statistic Δ_{surf} should be regarded as an estimate of heterogeneity, designed to provide a convenient summary of the results, other definitions are certainly possible.

The the comparison between the two thermal states shows that the surface variation between pairs of simulations is similar, therefore in this range of temperatures the surface variation is independent on the initial thermal state chosen (Figure S3). In all cases the two simulations resulted in close surface variation values ($|\Delta_{\text{surf,hot}} - \Delta_{\text{surf,cold}}| < 0.1$).

Corresponding author: R. Rufu, raluca@boulder.swri.edu

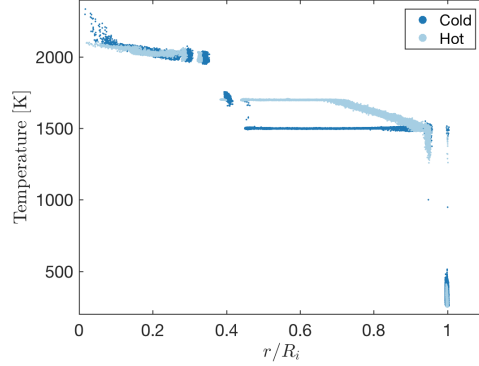


Figure S1: Initial profile temperatures as a function of the distance from the center, normalized by the radius of the moonlet, R_i .

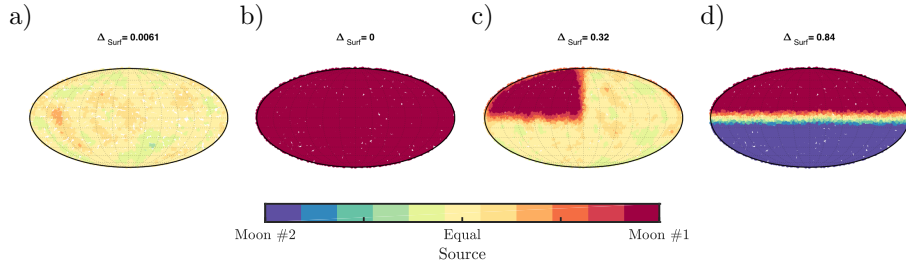


Figure S2: Surface variations across artificially generated surfaces. Small values of surface variation result from surfaces that are well mixed between the two sources (a) or surfaces that are sourced from one body (b). Large values of surface variation result from surfaces that include material from both sources but their material is unmixed, creating regions where material is unproportionally sourced (c, d)

The majority of mantle particles in the "hot" initial thermal state are closer to the melting point, hence less energy is required for melting (Figure S4). As expected, it has higher fractions of melt, compared to the "cold" initial state. However, for low velocity and hit-and-run impacts the difference between the two states is low (Figure S5). For accretionary impacts ($V_{\text{imp}} \sim V_{\text{esc}}$ in Figure S5), where deformation is abundant, the amount of melted material at the end of the simulation is significantly higher (highest difference value ~ 0.1). As the differences between the two thermal states are smaller compared to the differences between the impacts parameters, we chose to focus on the "cold" initial state.

Text S2 - Surface Variation Sensitivity Tests

To find the suitable neighborhood length that describes the large scale surface variations (differences between quadrants), we calculated the surface variation for the case depicted in Figure 6-d, assuming a range of values, $L_{\text{neighbour}} = 50 - 1000$ km. Using small $L_{\text{neighbour}}$, order of magnitude of smoothing length, most particles have small number of neighbours, therefore large scale surface variations are not resolved (*e.g.*, Figure S6 - b $L_{\text{neighbour}} = 50$ km). By increasing $L_{\text{neighbour}}$ each particle samples more neighbours (*e.g.*, for $L_{\text{neighbour}} = 200$ km case, typically each particle has 20-30 neighbours) and larger scale heterogeneities are resolved (*e.g.*, Figure S6-b for

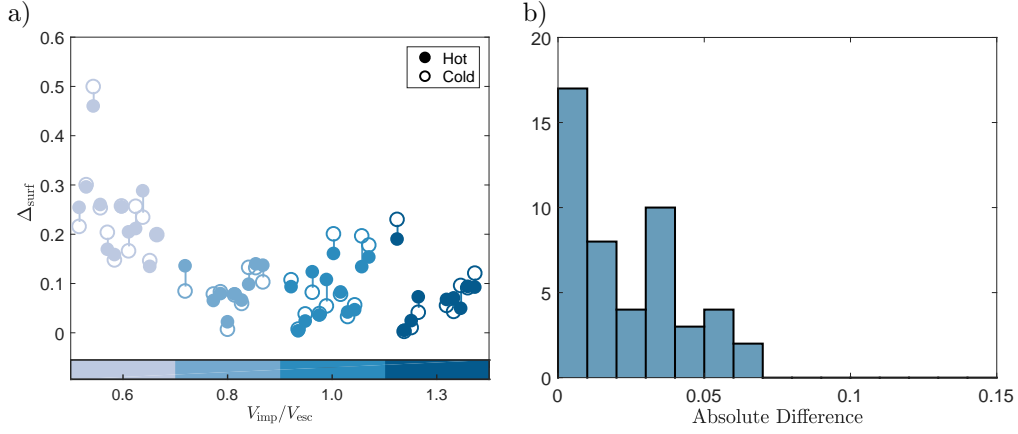


Figure S3: Surface variation difference between two simulations with different thermal states. a) Variation values (Δ_{surf}) of same impact conditions but different initial thermal state. Filled/empty circles represent the hot/cold initial thermal state. Colors represent the impact velocities. The vertical line represents the difference between the two simulations. b) Distribution of absolute surface heterogeneity difference between the two states ($|\Delta_{\text{surf,hot}} - \Delta_{\text{surf,cold}}|$).

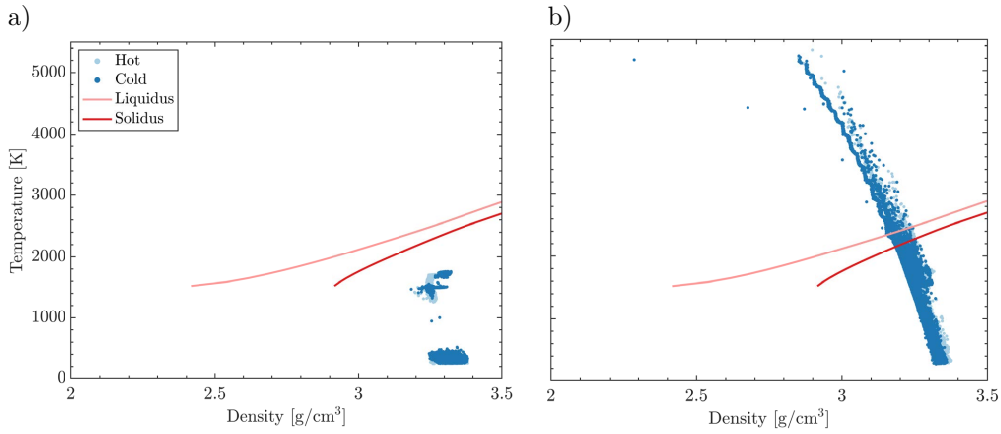


Figure S4: Thermal state of SPH particles. Temperature as a function of density at the a) beginning; b) end of simulation for the largest surviving remnant in a hit-and-run simulation. The dark/light red curves represent the solidus/liquidus curve, calculated by the M-ANEOS code [Melosh, 2007] (input parameters provided by J. Melosh) .

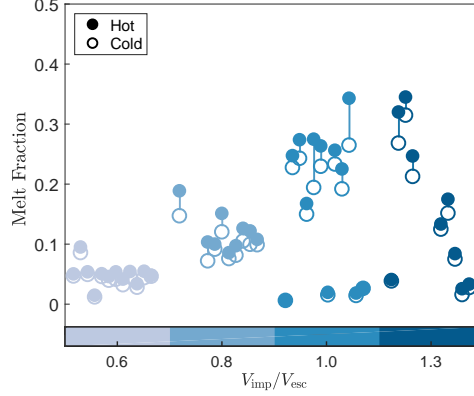


Figure S5: Melting fraction difference between two simulation with two different initial states but same impact conditions. Filled/empty circles represent the hot/cold initial thermal state. Colors represent the impact velocities. The vertical line represents the difference between the two simulations.

$L_{\text{neighbour}} = 200$ km, difference in source material between equatorial and pole region). Surface variation values between 250 – 700 km have a small dependence on the $L_{\text{neighbour}}$ chosen, whereas for larger values of the neighborhood length the heterogeneity values decrease (Figure S6-a). This is not surprising as when the neighbourhood length approaches similar scales to the radius of the moonlet, particles sample too many neighbours, and dichotomies between quadrants are barely resolved. As heterogeneity values do not depend strongly on the neighborhood length chosen for $L_{\text{neighbour}} = 250 - 700$ km, we chose to use the $L_{\text{neighbour}} = 400$ km value for our surface variation analysis.

In order to ensure that the the nominal resolution (number of SPH particles, $N_{\text{par}} \sim 2 \cdot 10^5$) is appropriate for estimating the surface variations, we performed additional impact simulations with varying number of SPH particles ($N_{\text{par}} \sim 2 \cdot 10^4$, $1 \cdot 10^5$ and $4 \cdot 10^5$). For ease of comparison, we chose to reproduce one of the impacts that resulted in some degree of heterogeneity (impact between two-half-moon sized bodies with a low impact velocity, $V_{\text{imp}} = 0.9V_{\text{esc}}$, and angle, $\beta = 21^\circ$). These tests show that the pattern of the surface mixing variations remains constant with number of particles $\geq 10^5$ (Figure S7). The amplitude of the mixing variations is somewhat reduced in the highest resolution case ($N \sim 4 \cdot 10^5$), but here too, the pattern is maintained (Figure S7-left panel - first row; surface material at high latitudes is unmixed). We conclude that simulations that show a high degree of mixing between the moonlets will remain so at higher resolution; increasing the number of particles is likely only to strengthen this result.

We note that, in the main text we have defined the surface particles as the upper 5% particles in each longitude-latitude rectangle of $15^\circ \times 15^\circ$. According to this definition, the surface is represented by $\mathcal{O}(10^3)$ particles, and sample particles as deep as 80 km for the nominal resolution. It allows a fast calculation of neighbouring particles and hence the surface mixing. However, it does not systematically sample the same depth for each longitude-latitude rectangle. Therefore, we made an additional test and calculated the mixing of all particles in the upper 50 km layer. According to this definition, the surface is represented by $\mathcal{O}(10^4)$ particles in the nominal resolution ($2 \cdot 10^5$ particles), and ensures that the sampling depth is consistent when the number of particles varies. However this technique, drastically increases the computational time of the neighboring particle search. We verified that the two surface definitions

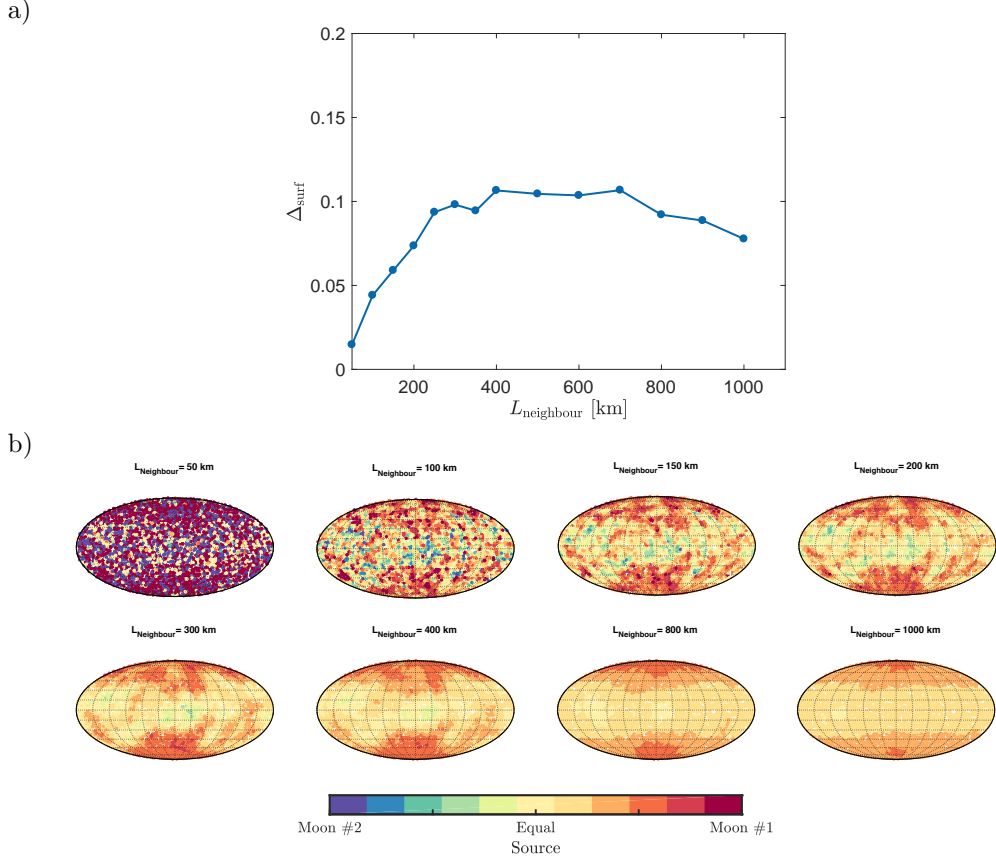


Figure S6: Sensitivity analysis on cases depicted in Figure 6-c4. a) Surface variation values defined by Eq. 1 vs. the neighbourhood length, $L_{\text{neighbour}}$; b) Source material from each moonlet for every surface particle. For the main manuscript we use the $L_{\text{neighbour}} = 400$ km

are consistent by comparing the Δ_{surf} values on a subset of our nominal resolution ($\gamma = 0.5$, 90 simulations), and find that the surface variations values are similar within $|\Delta_{\text{surf}} < 0.1|$. Finally, the variations among the different resolutions (Figure S7; second row) show a similar trend as before.

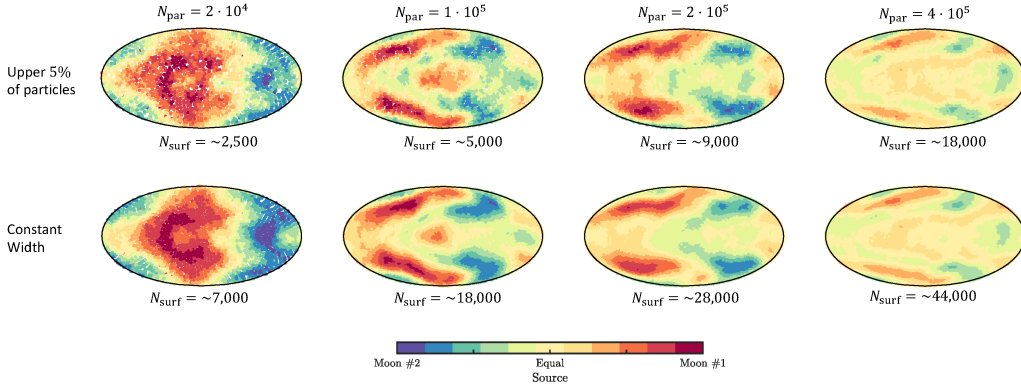


Figure S7: Resolution analysis. Source material on final moon, resulting from an impact between two-half-moon sized bodies with a low impact velocity and angle ($V_{\text{imp}} = 0.9 V_{\text{esc}}$; $\beta = 21^\circ$) with varying number of SPH particles, N_{par} (detailed on top of each column). The surface is defined as the upper 5% particles in each longitude-latitude rectangle of $15^\circ \times 15^\circ$ (first row) or the upper 50 km layer (second row). The surface variation value, Δ_{surf} , and the number of surface particles, N_{surf} , is detailed below each subpanel.

Caption Movie S1

Evolution of a sequence of two hit-and-run impacts. The two-half moonlets impact at a distance of $1.5 R_{\text{Roche}}$ from the planet (first impact: $\beta = 40^\circ$; $V_{\text{imp}} = 1.66 V_{\text{esc}}$; second impact: $\beta = 44^\circ$; $V_{\text{imp}} = 1.56 V_{\text{esc}}$). The planet (Roche limit) is represented by the green circle (dashed line), whereas the different color bars represent the entropy of the material originating from different moonlets. After the first impact, the two moonlets remain on similar, interacting orbits and the impact again at ~ 57 hr. After the second impact, moon#2 is scattered towards the Roche limit, where it disrupts. All projections are on the equatorial plane with one hemisphere removed. The upper left panel focuses on the surviving moonlet (Moon #1).

Caption Movie S2

Melt evolution of a sequence of two hit-and-run impacts. Snapshots of two colliding half moonlets at a distance of $1.5 R_{\text{Roche}}$ from the planet (first impact: $\beta = 40^\circ$; $V_{\text{imp}} = 1.66 V_{\text{esc}}$; second impact: $\beta = 44^\circ$; $V_{\text{imp}} = 1.56 V_{\text{esc}}$). The movie shows a slice of width 100 km centered in the equatorial plane of the largest surviving moon. The blue particles represent iron material and light/dark red particles represent the unmelted/melted magma material. Note that for emphasizing purposes, the melted particles are larger. In the first and second impact, melt is created mainly in the secondary stage of the impact, where material falls back to the surface.

References

- Barr, A. C. (2016), On the origin of Earth’s Moon, *Journal of Geophysical Research: Planets*, 121(9), 1573–1601.
- Canup, R. M. (2004), Dynamics of lunar formation, *Annual Review of Astronomy and Astrophysics*, 42(1), 441–475.
- Canup, R. M., H. F. Levison, and G. R. Stewart (1999), Evolution of a terrestrial multiple-moon system, *The Astronomical Journal*, 117(1), 603.

- Elkins-Tanton, L. T., S. Burgess, and Q.-Z. Yin (2011), The lunar magma ocean: Reconciling the solidification process with lunar petrology and geochronology, *Earth and Planetary Science Letters*, *304*(3), 326–336.
- Laneuville, M., M. A. Wieczorek, D. Breuer, and N. Tosi (2013), Asymmetric thermal evolution of the Moon, *Journal of Geophysical Research: Planets*, *118*(7), 1435–1452.
- Melosh, H. (2007), A hydrocode equation of state for SiO₂, *Meteoritics & Planetary Science*, *42*(12), 2079–2098.